

# Modeling the Neonatal Brain Development Using Implicit Neural Representations

Florentin Bieder<sup>1</sup>[0000-0001-9558-0623] [florentin.bieder@unibas.ch](mailto:florentin.bieder@unibas.ch),  
Paul Friedrich<sup>1</sup>[0000-0003-3653-5624] [paul.friedrich@unibas.ch](mailto:paul.friedrich@unibas.ch),  
Hélène Corbaz<sup>1</sup>[0009-0006-9716-5136] [helene.corbaz@unibas.ch](mailto:helene.corbaz@unibas.ch),  
Alicia Durrer<sup>1</sup>[0009-0007-8970-909X] [alicia.durrer@unibas.ch](mailto:alicia.durrer@unibas.ch),  
Julia Wolleb<sup>1</sup>[0000-0003-4087-5920] [julia.wolleb@unibas.ch](mailto:julia.wolleb@unibas.ch),  
and Philippe C. Cattin<sup>1</sup>[0000-0001-8785-2713] [philippe.cattin@unibas.ch](mailto:philippe.cattin@unibas.ch)

Department of Biomedical Engineering, University of Basel

**Abstract.** The human brain undergoes rapid development during the third trimester of pregnancy. In this work, we model the neonatal development of the infant brain in this age range. As a basis, we use MR images of preterm- and term-birth neonates from the developing human connectome project (dHCP). We propose a neural network, specifically an implicit neural representation (INR), to predict 2D- and 3D images of varying time points. In order to model a subject-specific development process, it is necessary to disentangle the age from the subjects' identity in the latent space of the INR. We propose two methods, Subject Specific Latent Vectors (SSL) and Stochastic Global Latent Augmentation (SGLA), enabling this disentanglement. We perform an analysis of the results and compare our proposed model to an age-conditioned denoising diffusion model as a baseline. We also show that our method can be applied in a memory-efficient way, which is especially important for 3D data. The code is available on <https://github.com/FlorentinBieder/Neonatal-Development-INR>.

**Keywords:** implicit neural representations, neonatal development, MRI

## 1 Introduction

The development of the central nervous system begins early in pregnancy and can be detected using ultrasound as early as eight weeks of gestation [14]. At around 20 weeks, the corpus callosum is fully developed, and the first structures of the cortical surface begin to form [15]. The process of cortical folding, or gyrification, continues well after term birth. Across most individuals, the gyrification is similar on a macroscopic level for the major structures, but differs on the level of the smaller sulci, even for monozygotic twins [2]. Before 20 weeks postmenstrual age (PMA) their brains' appearance have a high degree of similarity, but then progressively develop an individual character [25]. In this work, we try to model the subject specific development of the preterm and term neonatal brain, based on the dHCP dataset (see Section 3), containing brain MR images of neonates between 26 and 45 weeks PMA. This dataset poses challenges

due to limited data availability, with each subject having scans from at most two or three different points in time, and the majority having only a single scan available.

Using an implicit neural representation (INR), we want to predict the healthy brain development from a given scan at a given PMA. That is, we want to predict an image of the same subject at a later or earlier point in time. Therefore, we have to find an age-agnostic representation of the identity of the subject, meaning we need to disentangle the age from the identity to be able to represent the same subject at different points in time. Modelling the development of the healthy brain could then serve as a basis for further downstream tasks, e.g. detection of abnormal brain development. INRs work by representing images (and other signals) as networks that take the coordinates of a pixel as input and output the corresponding intensities. This is in contrast to convolutional neural networks (CNNs) or transformers, which process an entire image, i.e., a grid of pixels, at once. INRs have been successfully applied to the representation and modelling shapes [3,13], images [21], and recently also natural 3D scene reconstruction [20]. In the medical domain, they have been used for various tasks, such as image segmentation [22], shape completion [1], tomographic reconstruction [20,5], and image registration [23].

*Contribution* We show that an INR can be trained to model the neonatal brain development based on sparsely- and highly irregularly sampled data with respect to the time axis. Figure 1 provides an overview of the model. To enable the disentanglement along the time axis, we propose the following two methods that can be applied independently during training:

- A method to disentangle the subject’s PMA at the time of the scan from its identity by enforcing a subject-specific latent space (SSL).
- An augmentation method with a global latent vector in the latent space. We call it stochastic global latent augmentation (SGLA). This performs similarly to SSL but is intended to make better use of subjects with only a single scan in the dataset.

We show how SSL and SGLA can improve the disentanglement, and with that, the predictions. Furthermore, we show that our INR approach can be run on hardware with limited GPU memory.

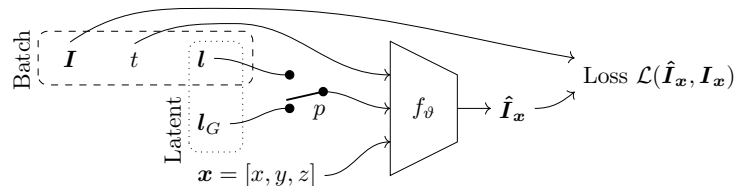


Fig. 1: Overview: The input to the network  $f_\theta$  consists of the spatial coordinates  $\mathbf{x}$  of the desired output pixel  $\hat{\mathbf{I}}_{\mathbf{x}}$ , the desired PMA  $t \in T$ , and a latent vector  $\mathbf{l} \in \mathcal{L}$ , encoding the subject identity. The switch with probability  $p$  between  $\mathbf{l}$  and the global latent vector  $\mathbf{l}_G$  represents the SGLA.

## 2 Method

This work presents an approach based on an INR. This means that we model our images  $\mathbf{I} \in \mathcal{I} = \{I : \Omega \rightarrow [0, 1]\}$  at different points of time  $t \in T$  as a function  $f_\vartheta : \Omega \times T \times \Lambda \rightarrow [0, 1]$  parametrized by  $\vartheta$ , where  $\Omega \subset \mathbb{R}^d$  is the spatial image domain,  $T = [0, 1]$  is the time domain (i.e. normalized PMA), and  $\Lambda \subset \mathbb{R}^\lambda$  is our latent space. For any image  $\mathbf{I} \in \mathcal{I}$  we denote the intensity at  $\mathbf{x} \in \Omega$  as  $\mathbf{I}_\mathbf{x}$ . In the forward pass, for each pixel, the normalized input coordinates  $\mathbf{x} \in \Omega$  are concatenated with the latent vector  $\mathbf{l}$  and the corresponding PMA  $t$  and then passed to the network. Therefore, during training, for some given image  $\mathbf{I}$  with corresponding PMA  $t$  and latent vector  $\mathbf{l}$ , and some input coordinates  $\mathbf{x}$ , we predict  $\hat{\mathbf{I}}_\mathbf{x} := f_\vartheta(\mathbf{x}, t, \mathbf{l})$ , and we optimize the  $\ell^2$ -loss  $\mathcal{L}(\hat{\mathbf{I}}_\mathbf{x}, \mathbf{I}_\mathbf{x}) = \|\hat{\mathbf{I}}_\mathbf{x} - \mathbf{I}_\mathbf{x}\|_2^2$  with respect to  $\vartheta$  and  $\mathbf{l}$ . This is described in more detail in Section 2.2. For inference, we can project an input image into the latent space by optimizing the latent vector with respect to the reconstructed image. To then predict images  $\hat{\mathbf{I}}^i$  for different points of time  $t_i$ , for a given latent vector  $\mathbf{l}$ , we can sample  $\hat{\mathbf{I}}_\mathbf{x}^i := f_\vartheta(\mathbf{x}, t_i, \mathbf{l})$  over the whole image domain  $\mathbf{x} \in \Omega$  for every  $t_i$ . This is described in detail in Section 2.2. The architecture of the network  $f_\vartheta$  is described in Appendix A.

### 2.1 Age Disentanglement in the Latent Space

In our setup, the latent space represents the identity of a subject. We want to disentangle the identity of the subject from its age. To this end, we propose the following two methods, which can be employed independently of each other:

*Subject Specific Latent Vectors (SSL)* Previously developed INRs for similar tasks use one latent vector per input image [1,22,3,13]. This is sufficient if we want our network to model a specific input image. In our case, we want the model to generalize the representation of a specific subject across the time domain  $T$  and to encode the subject’s identity independently, i.e., disentangle the identity from the age. Given the availability of images from multiple time points for one subject, we propose using the *same* latent vector for all images of the *same* subject, with the goal of forcing the model to use only the age inputs  $t \in T$  to encode the age of the subject and use the latent vector for encoding the identity of the subject only.

*Stochastic Global Latent Augmentation (SGLA)* The second method we propose for disentangling the subjects’ age from their identity is based on a specific type of data augmentation during training: We introduce an additional *global* latent vector  $\mathbf{l}_G$  for training. In each iteration of the stochastic gradient descent, the latent vector of the current batch is replaced with this global latent vector  $\mathbf{l}_G$  with some probability  $p$ . It is intended to mimic SSL for those subjects that have only a *single* scan in the dataset: Similarly as in SSL, the network is trained to predict scans at different developmental stages for the same latent vector. Instead of a subject specific latent vector, we use the global vector  $\mathbf{l}_G$  instead. This forces the network to take the age input  $t$  into account. We set the probability  $p=10\%$  to make it comparable to SSL, as about 10% of the subjects in the training set have more than one scan. We have performed an ablation with respect to  $p$  in Appendix D.1.

## 2.2 Training & Inference

The network, along with the latent vectors of the training set, is jointly optimized using the *AdamW* optimizer [11] with a learning rate of  $\text{lr} = 10^{-4}$  and an  $\ell_2$ -loss. Since the INRs can be processed pixel by pixel, we do not necessarily need to use the whole image for each training step. In our model, we can adjust the percentage of pixels that we randomly sample from a given image in each training step by a hyperparameter. We chose to use 5% for our experiments to fit the training of the 3D INRs on a GPU with 12GB memory. For simplicity, we used identical settings for the 2D case. This lets us easily adjust for the available memory size of a given GPU. The details of the pixel sampling are described in Appendix D.2

If we want to use the entire image (be it for training or inference), we can still profit from the pixel-wise evaluations: We can serialize the whole input into micro-batches that are processed sequentially and accumulate the gradients with a constant amount of memory. We use this for the inference of the 3D images. The amount of memory used is then mainly dictated by the micro-batch size. These methods allow us to train models on devices with very little memory. We discuss the resource consumption in Section 3.

*Inference* During inference, we use the same loss as during training, but we keep the network fixed and only optimize the latent vector  $\mathbf{l}$ . Therefore, for a given image  $\mathbf{I}^1$  with age  $t_1$  as input, we optimize a latent vector  $\mathbf{l}$  to minimize the difference between reconstruction  $\hat{\mathbf{I}}_{\mathbf{x}}^1 = f_{\vartheta}(\mathbf{x}, t_1, \mathbf{l})$  and the image  $\mathbf{I}_{\mathbf{x}}^1$  over all  $\mathbf{x} \in \Omega$ , i.e.  $\hat{\mathbf{l}} := \arg\min_{\mathbf{l} \in \Lambda} \sum_{\mathbf{x} \in \Omega} \|f_{\vartheta}(\mathbf{x}, t_1, \mathbf{l}) - \mathbf{I}_{\mathbf{x}}^1\|_2^2$ . We then use this vector  $\hat{\mathbf{l}} \in \Lambda$  to generate a prediction  $\hat{\mathbf{I}}$  for some desired age  $t_2 \in T$  by computing  $\hat{\mathbf{I}}_{\mathbf{x}} = f_{\vartheta}(\mathbf{x}, t_2, \hat{\mathbf{l}})$ . The latent vectors are initialized with zeros and then optimized over 1000 step for the 3D case and 2000 for the 2D case, using *AdamW* with a learning rate of  $\text{lr} = 10^{-3}$ .

## 2.3 Baseline: Denoising Diffusion Models

As a baseline, we use a denoising diffusion model with gradient guidance (DDM+GG) [26] to predict an image for a certain PMA, given some image of a different PMA. This method has been implemented for 2D images and has been shown to perform well on similar tasks such transforming portraits into younger or older versions, and simulating tumor growth over time.

DDM + GG uses two networks in tandem: the denoising and the regression network. The age conditioning is performed using the gradients of a regression network during the denoising process, which is trained to predict the subject’s PMA. The denoising and the regression networks were trained to convergence (1M and 150k iterations, respectively) with  $T = 1000$  noising and denoising steps. The number of noising and denoising steps for inference was  $L = 600$  and the gradient scale  $c = 3 \cdot 10^5$ . We optimized both parameters  $L$  and  $c$  on the test set to make a fair comparison. Since this method was proposed for 2D images, we also trained our INR on the same 2D data (axial slices). The details are reported in Appendix B.

### 3 Experiments & Results

In the following section, we report the results of our experiments. If not otherwise noted, the setup is as follows: From each subject in the test set, we consider two scans that were made at a different point of time, i.e., at a different PMA of the subject. As explained in Section 2.2, for a given subject, we first determine the latent vector  $\hat{\mathbf{l}}$  based on the input image  $\mathbf{I}^1$  and PMA  $t_1$ , that is, we optimize  $\hat{\mathbf{l}} := \operatorname{argmin}_{\mathbf{l} \in \mathcal{A}} \sum_{x \in \Omega} \|f_{\vartheta}(\mathbf{x}, t_1, \mathbf{l}) - \mathbf{I}_x^1\|_2^2$ . We then use this latent vector  $\hat{\mathbf{l}}$  to generate a prediction  $\hat{\mathbf{I}}$  for the PMA  $t_2$  of the second scan  $\mathbf{I}^2$  by computing  $\hat{\mathbf{I}}_x^2 := f_{\vartheta}(\mathbf{x}, t_2, \hat{\mathbf{l}})$  for every  $x \in \Omega$ . We then compare the predicted image  $\hat{\mathbf{I}}$  with the second scan  $\mathbf{I}^2$ , which serves as the ground truth for all metrics that we will introduce below. This allows us to quantify how well our model predicts the development process of the brain. To justify our contributions, we perform an ablation of our proposed method, that is, we conduct our experiments with and without SGLA and SSL, respectively, in 2D as well as in 3D.

*Dataset* We used the dHCP (third data release) dataset for our experiments [12,2]. It contains  $T1$ - and  $T2$ -weighted neonatal MR-scans of 329 subjects. We use the  $T2$ -weighted scans as these are preferred for assessing brain structure in fetal and neonatal MRI [12], due to the immature myelination. The postmenstrual age (PMA, in weeks) is available for each scan, ranging from 26 to 45 weeks with a median of 40.57. Our preprocessing is described in Appendix C.

*Ablation of SSL and SGLA and comparison to the Baseline* To compare our predictions on the test set with the corresponding ground truths, we compute the peak-signal-noise-ratio (PSNR), the structural similarity index (SSIM) and the mean absolute error (MAE). We report the same metrics for the baseline DDM+GG in Table 1. Our proposed 2D INR with SGLA and SSL outperforms DDM+GG with respect to every metric. Furthermore, the performance decreases without SGLA or SSL (or neither). However, it should be noted that in the 2D case we only consider a slice of the 3D volume. Much of the anatomical context is therefore missing, making it more difficult to predict changes that are influenced by tissue not shown on the slice in question. For this purpose, we train our INR model on the 3D volumes as a whole and perform the same ablation of SGLA and SSL again. The results are reported in Table 1. The difference between the different models in terms of PSNR, SSIM and MAE is relatively small in absolute terms, because the image background is black, which is easy to predict for a model. In other words, if the background remains constant and only the foreground improves, this reduces the effect on these scores. However, we can still see that both SSL and SGLA improve all three scores. Furthermore, even in the presence of a number of subjects with multiple scans available, SGLA can be used in conjunction with SSL and still improve the performance, in 2D as well as in 3D.

In addition to the three metrics we use in the 2D case, in the 3D case, we can compute the head circumference (HC) based on our predictions (details in Appendix E). Along with several other measurements, the HC is one of the most important factors in determining prenatal development [10]. Therefore, we used it to measure how well our proposed method performs concerning the disentanglement of the subjects' age. We compare the measured HC of our predictions with the HC reported in the dHCP

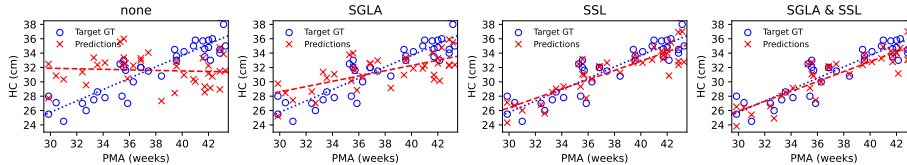
dataset, which we consider the ground truth. Table 1 displays the standard deviation  $\sigma$  (in cm) of the error between the measured HC of our prediction and the ground truth. Furthermore, we report the correlation coefficient  $r$  between the predicted HC and the ground truth HC. Notably, we can see that with neither SGLA nor SSL, the HCs of the predictions are almost uncorrelated with the ground truth HCs. Again, our proposed INR with SGLA and SSL outperforms the other ablated models in each of these measures or performs at least as well.

Table 1: Average scores over the test set for the 2D INRs and the 2D DDM+GG baseline, as well as for the 3D INRs.

Model			2D			3D			HC $\sigma$	HC $r$
	SGLA	SSL	PSNR	SSIM	MAE	PSNR	SSIM	MAE		
INR	n	n	19.5±2.6	0.642±0.058	0.0701±0.0178	22.9±3.1	0.804±0.036	0.0352±0.0091	3.850	0.173
	y	n	20.6±2.5	0.683±0.065	0.0571±0.0146	23.8±2.8	0.832±0.049	0.0274±0.0083	2.137	0.835
	n	y	21.3±2.1	0.715±0.075	0.0489±0.0124	24.5±2.4	0.850±0.054	0.0232±0.0079	1.071	0.962
	y	y	<b>21.4±2.0</b>	<b>0.722±0.075</b>	<b>0.0468±0.0129</b>	<b>24.6±2.4</b>	<b>0.853±0.055</b>	<b>0.0225±0.0078</b>	<b>0.964</b>	<b>0.968</b>
DDM+GG	-	-	19.3±2.1	0.632±0.088	0.0682±0.0158	-	-	-	-	-

To better understand these results, we plot the ground truth HC and the measured HC of our predictions in Figure 2 for all four INRs. We can see that the INR with neither SGLA nor SSL completely fails to capture the developmental process. Using either SGLA or SSL significantly improves the correlation between the HC of the prediction and the ground truth HC. Finally using both jointly enables the model to capture the development process even better.

Fig. 2: Ablation of our model w.r.t. the HC. The blue circles show the HC ground truth, while the red x-es show the HC of our models’ predictions on the test set.



*Qualitative Results* In Figure 3, we show two examples from the test set. We show four images per subject: (1) the *input*  $I^1$  with its age  $t_1$  that gets encoded into a latent vector, (2) the reconstruction  $\hat{I}^1$  of the input at  $t_1$ , (3) the *target ground truth*  $I^2$  from  $t_2$  and (4) the prediction  $\hat{I}^2$  at age  $t_2$ . Note that for our model,  $t_2$  does not necessarily have to be greater than  $t_1$ , we can also choose to look back in time to predict what a given brain has looked like in the past. The reconstructions display the input images with some loss of details due to the bottleneck created by the low-dimensional latent space. The predictions generally match the size and the contrast of the target ground truth well, but have trouble predicting the exact shape of the cortical folds. This is, however, a difficult task, as even for monozygotic twins, the folds exhibit individual

patterns [25]. On the bottom right, we see an interesting example where the mid-sagittal plane of the input is slightly off the vertical, in contrast to the target ground truth. Interestingly, however, the reconstruction, as well as the prediction, display this slight rotation, which means it must have been encoded in the latent vector.

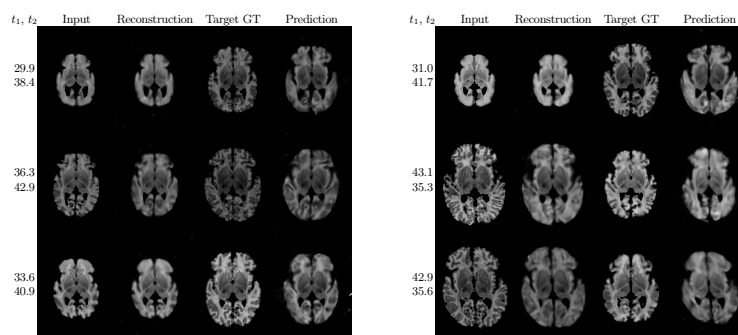


Fig. 3: Six examples from the test set, along with the PMA  $t_1$  of the input, and the PMA  $t_2$  of the target ground truth image.

*Predicted Average Development* To gain insight into the development process that the trained network captured, we consider two methods of extracting an “average” brain for each age, similar to creating an age-resolved atlas. Firstly, since we have designed the latent space to represent the characteristics of a subject, it can be expected that averaging the latent vectors of a population (i.e., our training set) would result in an average-looking brain. Secondly, because we initialize the latent vectors with a zero-vector, it is also possible to use it for the generation of an “average” brain. Thus, we use these two (*zero-* and *average-*) latent vectors to generate a temporal sequence of images of the trained model with SSL and SGLA. Furthermore, we compare the two approaches with the IMAGINE fetal atlas [8], as well as the neonatal atlas of Schuh et al. [19]. The latter is also based on the dHCP dataset. In Figure 4, we report the measured HCs along with percentiles of a fetal-infant preterm growth chart [6,7]. For instance, for diagnosing microcephaly, bounds like the 1<sup>st</sup> or 3<sup>rd</sup> percentile or three standard deviations of the HC are being used [4]. Under these criteria, all four growth curves are within the normal range. Notably, the HC lines of our generated “average”-brains agree very well with the atlas of [19], which is based on the same dataset. The IMAGINE atlas [8], exhibits slightly larger HCs, but is created using a set of *fetal* MR-images, with a significantly smaller sample size of 81 scans. However, it also remains within the normal interval. The quality of the two generated sequences using the zero- and average latent vector is different: The series generated by the average latent vector is more detailed and has less blurry features.

*Computational Resources* In Table 2, we report the time and GPU memory used. We used the same settings regarding pixel-sampling and micro-batching for the 2D- and

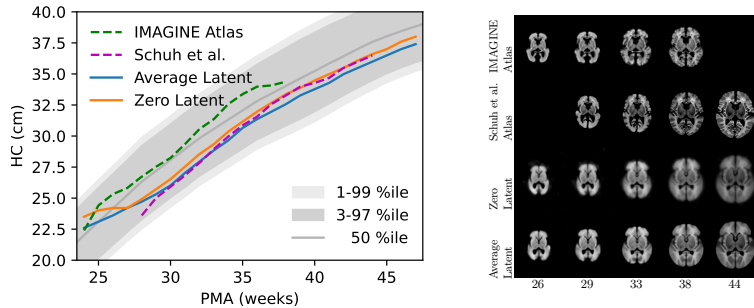


Fig. 4: Comparison of our “average” brain development with the IMAGINE atlas and the atlas of Schuh et al. in terms of HC growth curves Figure 4a, along with the quantiles reported in [6]. Furthermore, we show the corresponding axial slices in Figure 4b.

3D case. As elaborated in Section 2.2, we can reduce the number of pixels sampled per optimization step. Alternatively, we have the option to use micro-batching to trade memory for time. Finally, the number of parameters used in the 2D and 3D INRs is more than two orders of magnitude smaller than in the 2D DDM+GG baseline.

Table 2: Resources used for the INRs in 2D and 3D and the DDM+GG baseline.

Model	GPU Memory (in MB)		Time		# Parameters
	Training	Inference	Training (total)	Inference (per Sample)	
INR 3D	10350	10286	81.6 h	5.20 min	232 450
INR 2D	284	232	2.5 h	0.73 min	232 194
DDM 2D	7412	1332	76.8 h	1.80 min	113 669 762
Regression 2D	6412		7.9 h		86 786 817

## 4 Conclusion

We present a method for modelling the neonatal brain development using INRs. We show that it is necessary to disentangle the subject’s identity from its age. We propose and evaluate two novel methods, SSL and SGLA. We implement them in 2D as well as in 3D. On the one hand, we compare the predictions with the ground truth with respect to image quality, and on the other hand also indirectly via the HC as an important development metric. We demonstrate how our two proposed solutions improve the results through the disentanglement. However, we note that the image synthesis with INRs still has open challenges such as the image quality, and the modelling of processes like the cortical folding, which are additionally influenced by other factors than time. We anticipate that larger datasets would enable more



expressive networks to be trained, which could in turn alleviate these issues to some degree. To avoid the need for coregistration of the scans as a preprocessing step, it would be interesting to extend the disentanglement also to geometric transformations. In future work, we would like to explore extending the model to predict segmentations, which could be used to generate actual atlases.

**Acknowledgments.** We are grateful for the support of the Novartis FreeNovation initiative and the Uniscientia Foundation (project #147-2018). We would also like to thank the NVIDIA Corporation for donating a GPU that was used for our experiments.

Data were provided by the developing Human Connectome Project, KCL-Imperial-Oxford Consortium funded by the European Research Council under the European Union Seventh Framework Programme (FP/2007-2013) / ERC Grant Agreement no. [319456]. We are grateful to the families who generously supported this trial.

**Disclosure of Interests.** The authors have no competing interests to declare that are relevant to the content of this article.

## References

1. Amiranashvili, T., Lüdke, D., Li, H.B., Menze, B., Zachow, S.: Learning shape reconstruction from sparse measurements with neural implicit functions. In: International Conference on Medical Imaging with Deep Learning. pp. 22–34. PMLR (2022)
2. Bozek, J., Makropoulos, A., Schuh, A., Fitzgibbon, S., Wright, R., Glasser, M.F., Coalson, T.S., O’Muircheartaigh, J., Hutter, J., Price, A.N., et al.: Construction of a neonatal cortical surface atlas using multimodal surface matching in the developing human connectome project. *NeuroImage* **179**, 11–29 (2018)
3. Chen, Z., Zhang, H.: Learning implicit fields for generative shape modeling. In: Proceedings of the IEEE/CVF Conference on Computer Vision and Pattern Recognition. pp. 5939–5948 (2019)
4. DeSilva, M., Munoz, F.M., Sell, E., Marshall, H., Kawai, A.T., Kachikis, A., Heath, P., Klein, N.P., Oleske, J.M., Jehan, F., et al.: Congenital microcephaly: case definition & guidelines for data collection, analysis, and presentation of safety data after maternal immunisation. *Vaccine* **35**(48Part A), 6472 (2017)
5. Fang, Y., Mei, L., Li, C., Liu, Y., Wang, W., Cui, Z., Shen, D.: Snaf: Sparse-view cbct reconstruction with neural attenuation fields. arXiv preprint arXiv:2211.17048 (2022)
6. Fenton, T.R.: A new growth chart for preterm babies: Babson and benda’s chart updated with recent data and a new format. *BMC pediatrics* **3**, 1–10 (2003)
7. Fenton, T., Sauve, R.: Using the lms method to calculate z-scores for the fenton preterm infant growth chart. *European journal of clinical nutrition* **61**(12), 1380–1385 (2007)
8. Gholipour, A., Rollins, C.K., Velasco-Annis, C., Ouaalam, A., Akhondi-Asl, A., Afacan, O., Ortinau, C.M., Clancy, S., Limperopoulos, C., Yang, E., et al.: A normative spatiotemporal mri atlas of the fetal brain for automatic segmentation and analysis of early brain growth. *Scientific reports* **7**(1), 476 (2017)
9. He, K., Zhang, X., Ren, S., Sun, J.: Deep Residual Learning for Image Recognition. In: Proceedings of the IEEE Conference on Computer Vision and Pattern Recognition (CVPR) (June 2016)
10. Kiserud, T., Piaggio, G., Caroli, G., Widmer, M., Carvalho, J., Neerup Jensen, L., Giordano, D., Cecatti, J.G., Abdel Aleem, H., Talegawkar, S.A., et al.: The world health organization fetal growth charts: a multinational longitudinal study of ultrasound biometric measurements and estimated fetal weight. *PLoS medicine* **14**(1), e1002220 (2017)

11. Loshchilov, I., Hutter, F.: Decoupled weight decay regularization. arXiv preprint arXiv:1711.05101 (2017)
12. Makropoulos, A., Robinson, E.C., Schuh, A., Wright, R., Fitzgibbon, S., Bozek, J., Counsell, S.J., Steinweg, J., Vecchiato, K., Passerat-Palmbach, J., et al.: The developing human connectome project: A minimal processing pipeline for neonatal cortical surface reconstruction. *Neuroimage* **173**, 88–112 (2018)
13. Mescheder, L., Oechsle, M., Niemeyer, M., Nowozin, S., Geiger, A.: Occupancy networks: Learning 3d reconstruction in function space. In: Proceedings of the IEEE/CVF conference on computer vision and pattern recognition. pp. 4460–4470 (2019)
14. Monteagudo, A., Timor-Tritsch, I.E.: Ultrasound of the fetal brain. *Ultrasound Clinics* **2**(2), 217–244 (2007)
15. Rubenstein, J., Rakic, P.: Patterning and cell type specification in the developing CNS and PNS: comprehensive developmental neuroscience, vol. 1. Academic Press (2013)
16. Salomon, L., Alfirevic, Z., Da Silva Costa, F., Deter, R., Figueras, F., Ghi, T.a., Glanc, P., Khalil, A., Lee, W., Napolitano, R., et al.: Isuog practice guidelines: ultrasound assessment of fetal biometry and growth. *Ultrasound in obstetrics & gynecology* **53**(6), 715–723 (2019)
17. Saragadam, V., LeJeune, D., Tan, J., Balakrishnan, G., Veeraraghavan, A., Baraniuk, R.G.: Wire: Wavelet implicit neural representations. In: Proceedings of the IEEE/CVF Conference on Computer Vision and Pattern Recognition. pp. 18507–18516 (2023)
18. Sarris, I., Ioannou, C., Chamberlain, P., Ohuma, E., Roseman, F., Hoch, L., Altman, D., Papageorgiou, A., Fetal, I., for the 21st Century (INTERGROWTH-21st), N.G.C.: Intra-and interobserver variability in fetal ultrasound measurements. *Ultrasound in obstetrics & gynecology* **39**(3), 266–273 (2012)
19. Schuh, A., Makropoulos, A., Robinson, E.C., Cordero-Grande, L., Hughes, E., Hutter, J., Price, A.N., Murgasova, M., Teixeira, R.P.A., Tusor, N., et al.: Unbiased construction of a temporally consistent morphological atlas of neonatal brain development. *BioRxiv* p. 251512 (2018)
20. Shen, L., Pauly, J., Xing, L.: Nerp: implicit neural representation learning with prior embedding for sparsely sampled image reconstruction. *IEEE Transactions on Neural Networks and Learning Systems* (2022)
21. Sitzmann, V., Martel, J., Bergman, A., Lindell, D., Wetzstein, G.: Implicit neural representations with periodic activation functions. *Advances in neural information processing systems* **33**, 7462–7473 (2020)
22. Stolt-Ansó, N., McGinnis, J., Pan, J., Hammernik, K., Rueckert, D.: Nisf: Neural implicit segmentation functions. In: International Conference on Medical Image Computing and Computer-Assisted Intervention. pp. 734–744. Springer (2023)
23. Sun, S., Han, K., Kong, D., You, C., Xie, X.: Mirnf: Medical image registration via neural fields. arXiv preprint arXiv:2206.03111 (2022)
24. Tuzikov, A.V., Colliot, O., Bloch, I.: Brain symmetry plane computation in mr images using inertia axes and optimization. In: 2002 International Conference on Pattern Recognition. vol. 1, pp. 516–519. IEEE (2002)
25. White, T., Su, S., Schmidt, M., Kao, C.Y., Sapiro, G.: The development of gyrification in childhood and adolescence. *Brain and cognition* **72**(1), 36–45 (2010)
26. Wolleb, J., Sandkühler, R., Bieder, F., Cattin, P.C.: The swiss army knife for image-to-image translation: Multi-task diffusion models. arXiv preprint arXiv:2204.02641 (2022)

## A Detailed Architecture

Our network  $f_\theta$  is built using affine blocks with WIRE [17] activations which are state-of-the-art for INRs, and have been shown to outperform the previously state-of-the-art SIREN networks [21] in many applications of INRs. They have the advantage of avoiding the additional complexity of positional encodings. We performed experiments using different residual topologies. Based on the subjective quality of the generated images on the training set, we chose to use a fully residual architecture, that also has been proposed in [22]. Specifically, we use a residual architecture with additive skip connections around each WIRE block with the same input and output dimension. Furthermore, we chose a network depth of nine layers, based on an ablation over the number of layers and the subjective appearance of the image quality during training.

More specifically, our network  $f_\theta$  is composed of multiple layers  $\varphi_i$ . Let  $h \in \mathbb{N}$  be the number of hidden dimensions,  $\lambda \in \mathbb{N}$  the latent dimension and  $d$  the number of spatial dimensions. The INR network is defined as

$$f_\theta = \varphi_N \circ \psi_{n-1} \circ \dots \circ \psi_2 \circ \varphi_1 \quad (1)$$

with residual blocks  $\psi_i(x) = \frac{1}{2}(x + \varphi_i(x))$ , similar as in [9]. Furthermore, the WIRE blocks are

$$\begin{aligned} \varphi_i: \mathbb{R}^{n_i} &\rightarrow \mathbb{R}^{m_i} \\ x &\mapsto \sin(\omega_0 u_i(x)) e^{-(s_0 v_i(x))^2} \end{aligned} \quad (2)$$

where  $u_i, v_i: \mathbb{R}^{n_i} \rightarrow \mathbb{R}^{m_i}$  are affine maps with trainable parameters. The application of the scalar functions to vectors is understood to be element-wise. In our case  $\lambda = m_1 = \dots = m_{N-1} = n_2 = \dots = n_N = h = 128$ ,  $m_N = 1$  and  $n_1 = \lambda + d + 1$  and  $d = 2$  for the 2D case, and  $d = 3$  for the 3D case.

## B Hyperparameter Optimization DDM+GG

To allow for a fair comparison, we optimized the parameters of the DDM+GG sampling on the test set via a grid search. First, we performed a visual inspection over a coarse grid of samples with  $c \in [10^5, 10^8]$  and  $L \in [100, 700]$ . Then, we performed a finer grid search and evaluated the metrics described in Section 3. The metrics are shown in Figure 5. We chose  $L = 600$  and  $c = 3 \cdot 10^5$ , as the PSNR metric was maximal in this case. The maximal SSIM was attained at  $L = 500$  with the same value of  $c$ , but overall, the SSIM metric seems to be a lot less sensitive to these two hyperparameters, which is why we prioritized the PSNR metric for this choice.

## C Preprocessing

We aligned the central (mid-sagittal) plane to the image axes. The mid-sagittal plane was determined by rigidly registering the images to their mirror image, as proposed in [24]. Then, we adjusted the orientation by registering the image to an average over the dataset with only intra-plane translations, rotations, and isotropic scaling. Finally, we undo the scaling from the registration to get back to the original size.

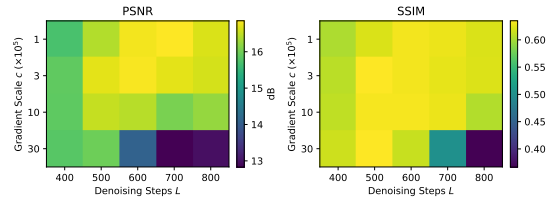


Fig. 5: PSNR and SSIM on the test set as a function of the number of noising and denoising steps  $L$  and the gradient scale  $c$  for the DDM+GG baseline [26].

We performed a skull-stripping that also removed all the cerebrospinal fluid (CSF), to avoid unnecessary hyperintense regions. The background voxels were set to zero, and the range between the first and 99th percentile of the foreground was normalized to  $[0,1]$ . For the training, we used 329 subjects with only a single scan and 19 subjects with two scans. For the validation, we used four subjects with two scans; for testing, we used another 19 subjects with two or more scans. After the preprocessing, we are left with volumes of dimension  $192 \times 256 \times 192$  with an isotropic voxel size of 0.588 mm. We normalize the spatial input coordinates to  $[-0.5,0.5]$ , and divide the temporal coordinates (i.e. PMA in weeks) by 100 to map them into the range  $[0,1]$ .

## D Hyperparameters of the INRs

### D.1 Ablation of $p$ parameter in SGLA

As outlined in Section 2 we chose  $p=10\%$ . To verify if this is optimal, we perform an ablation with respect to  $p$  in the range 0% to 25% and report  $\sigma$  and PSNR as in Section 3 in Figure 6. As already reported in Section 3, SGLA with  $p=10\%$  improves the predictions over the baseline without SGLA. In Figure 6 we see that it would probably be possible to marginally increase the performance, but for  $p > 10\%$  the improvements start to diminish.

### D.2 Foreground- to Background Ratio

If we were to sample the pixels uniformly from the given image during training, we would get a proportionally large amount of background pixels. We found that the uniform background is easy to learn for the network, while the foreground is more challenging. We therefore introduced a second hyperparameter, that sets a fixed ratio of foreground pixels to background pixels sampled per step. We set this ratio to 90:10 to favor the foreground. In the inference we use the same foreground to background ratio as in the training. For the 2D case we could afford to use all pixels in each optimization step of the inference.

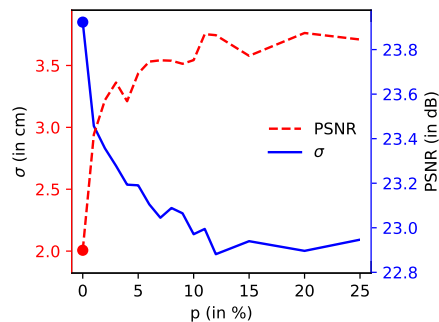


Fig. 6: Ablation of the probability parameter  $p$  for SGLA. We report  $\sigma$  and the PSNR as in Section 3. The dots indicate  $p=0$  i.e. when SGLA is not used.

## E Linking Head- & Brain Circumference

As we performed skull-stripping as a preprocessing step, it is not possible to measure the head circumference (HC) directly. The HC is usually estimated by measuring it with a flexible tape measure, or by measuring the occipitofrontal and biparietal diameters to define an ellipse. The HC is then estimated using the circumference [16] of said ellipse. Alternatively, it can also be measured using a flexible tape measure. In both cases, not choosing the correct plane in which the HC is measured can lead to errors.

We employ the latter method to get the brain circumference (BC) and perform a linear regression between measured BC and reported HC on the training set. As shown in Figure 7, these two values are highly correlated ( $r=0.9358$ ). The error has a standard deviation of  $\sigma=0.86$  cm. We use this linear model to predict the HC in our experiments, which means that this value should be considered a lower bound.

With this indirect method, a source of error is the relationship between BC and HC. Due to variations in thickness of the skull and the surrounding tissue, the linear model does not capture this relationship perfectly. Furthermore, as can be seen from the vertical clustering in Figure 7, some measurements appear more frequently than others. We estimate that about half of the measurements was rounded to 5 mm and about one third to 10 mm, while the rest was rounded to 1 mm.

To justify this, we compare the accuracy of this linear model with other errors reported in the literature, and point out some other error sources: The intra-observer standard deviation for the ellipse based HC measurement is 0.615 cm [18], which is slightly lower but comparable to the error we estimated for our method. It is, however, reported for sonography, and not for MRI, and with manual placement of the ellipse, but it still allows us to get a rough estimate of the error we can expect.

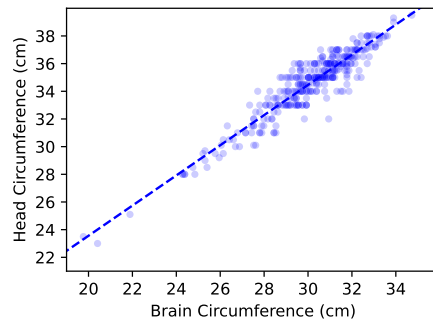


Fig. 7: Linear Regression between Brain- and Head circumference:  
 $HC = 1.090BC + 1.758$  cm,  $\sigma = 0.8600$  cm,  $r = 0.9358$